

Lunar Photoemission Yields Inferred From ARTEMIS Measurements

Key Points:

- We make the first report of oxygen Auger electron observations at the Moon by the Acceleration, Reconnection, Turbulence, and Electrodynamics of the Moon's Interaction with the Sun spacecraft
- We infer a lower bound of 10^{-3} in photoemission yield of the lunar surface for photon energies $> \sim 20$ eV
- Uncertainties over four orders of magnitude in yields are found, motivating future experiments on lunar samples for a better understanding

Supporting Information:

Supporting Information may be found in the online version of this article.





Correspondence to:

S. Xu,
shaosui.xu@ssl.berkeley.edu

Citation:

Xu, S., Poppe, A. R., Harada, Y., Halekas, J. S., & Chamberlin, P. C. (2021). Lunar photoemission yields inferred from ARTEMIS measurements. *Journal of Geophysical Research: Planets*, 126, e2020JE006790. <https://doi.org/10.1029/2020JE006790>

Received 30 NOV 2020
Accepted 11 MAY 2021

Shaosui Xu¹ , Andrew R. Poppe¹ , Yuki Harada² , Jasper S. Halekas³ , and Phillip C. Chamberlin⁴ 

¹Space Sciences Laboratory, University of California, Berkeley, CA, USA, ²Department of Geophysics, Kyoto University, Kyoto, Japan, ³Department of Physics and Astronomy, University of Iowa, Iowa City, IA, USA, ⁴Laboratory for Atmospheric and Space Physics, University of Colorado, Boulder, CO, USA

Abstract Photoemission yield (the number of emitted electrons per incoming photon) is one of the fundamental properties of solid materials but is not yet well constrained for the lunar surface for photon energies $> \sim 20$ eV. In this study, we constrain this yield for incident photons with energies of ~ 10 –500 eV with data from the Acceleration, Reconnection, Turbulence, and Electrodynamics of the Moon's Interaction with the Sun (ARTEMIS) mission along with solar irradiance spectra from Version 2 of the Flare Irradiance Spectral Model. We also report the first oxygen Auger electron observations at the Moon by the ARTEMIS spacecraft, which provides a unique feature to identify photoelectrons emitted from the lunar surface. With lunar photoelectron observations identified in both Earth's magnetotail lobes and the solar wind for four selected days, we infer a lower bound of 10^{-3} in yield for photon energies $> \sim 20$ eV. However, our investigation also reveals an uncertainty over ~ 4 orders of magnitude in derived yields with a sensitivity study, owing to a poorly constrained photoelectron energy probability function. This uncertainty motivates future experiments on lunar samples to better characterize the lunar surface charging environment.

Plain Language Summary The photoemission yield (the number of emitted electrons per incoming photon) is one of the fundamental properties of solid materials, but not yet well constrained for the lunar surface for photon energies $> \sim 20$ eV (electron volts). A better understanding of lunar surface photoemission yield is also important for characterizing the lunar electrostatic charging environment, as lunar photoelectrons contribute to one of the dominant currents at/near the lunar surface. This study utilizes measurements from the Acceleration, Reconnection, Turbulence, and Electrodynamics of the Moon's Interaction with the Sun mission and also full solar irradiance spectra from a model to determine this yield. While we can infer a lower bound in yield for photon energies $> \sim 20$ eV, we find an uncertainty over ~ 4 orders of magnitude in derived yields, which motivates future experiments on lunar samples to better characterize the yield function.

1. Introduction

Photoemission yield (or photoelectron yield, defined as the number of emitted electrons per incoming photon) is one of the fundamental properties of solid materials. Photoelectron yields vary over an order of magnitude at a given photon energy, depending on the surface materials (Feuerbacher et al., 1972), the degree of oxidation (Gard & Tunaley, 1971), the degree of structural disorder (e.g., crystalline vs. amorphous surfaces) (Willis et al., 1973), and the porosity/roughness of the surface (Dove et al., 2018; Feuerbacher et al., 1972; Gard, 1997). Laboratory measurements of lunar samples were conducted with photon energies from 4 to 21 eV to determine the work function and photoelectron yield function (Feuerbacher et al., 1972; Willis et al., 1973). The measured yield curve of lunar regolith increases exponentially from 10^{-6} at ~ 6 eV to a peak of 9% at 14 eV, falling to $\sim 1\%$ at 21 eV. This rapidly decreasing yield at higher energies is strikingly different from the yields of bulk insulators, which are constant or even increasing for energies $> \sim 10$ eV (Gard, 1997). For even higher-energy photons at ~ 100 –1,000 eV, yields of metals are relatively constant at $\sim 10\%$ (Cimino & Schäfers, 2014; Day et al., 1981; Willis et al., 1973), but photoelectron yields of lunar samples for extreme ultraviolet photons have not yet been measured. We also note that the photoelectric properties of the lunar samples returned to Earth could have been changed drastically by absorbed gaseous impurities (Willis et al., 1973). Thus, the structure of the regolith is likely not being perfectly preserved,

and the returned samples may not fully reproduce the average photoelectric properties of the lunar surface. Meanwhile, Reasoner and Burke (1972) presented lunar photoelectron energy spectra at ~ 40 – 200 eV measured at the Apollo 14 site on the lunar surface. However, the electron measurements on the lunar surface could have been contaminated by photoelectrons emitted from the instrument surface (see discussion in Reasoner & Burke, 1972). To exclude the possible influence of contamination and to validate the Apollo-era laboratory and surface measurements, clean, accurate, in-situ measurements of lunar photoemissivity with modern instrumentation are necessary.

A better understanding of lunar surface photoemission yield is important for characterizing the lunar electrostatic charging environment. The dayside surface electrostatic potential is determined by a current balance from different plasma populations at or accessible to the surface, such as ambient charged particles (e.g., the solar wind, the Earth's magnetosheath plasma, or Earth's lobe low-density plasma), particles photo-ionized by solar photons (e.g., Halekas et al., 2012; Poppe et al., 2012; Yokota et al., 2009), and secondaries produced by energetic particles (e.g., Halekas et al., 2009a; Manka, 1973). Depending on the ambient plasma density, different current terms dominate and control the surface potentials (e.g., Halekas et al., 2009b). In this study, we focus on two plasma regimes: (1) in the solar wind, the sunlit lunar surface is dominated by currents from the incoming ambient electrons and escaping photoelectrons, forming a positive potential sheath above the surface to balance the incoming electron flux and escaping photoelectron flux (e.g., Freeman & Ibrahim, 1975; Freeman et al., 1973), also see Figure 1 from Harada et al. (2017)). Inside the potential sheath, currents are dominated by low-energy photoelectrons (the cold core population) such that the dayside surface potential generally ranges from 0 to ~ 10 V (e.g., Halekas, Saito, et al., 2011; Halekas et al., 2008), and (2) in the magnetotail lobes, the ambient plasma density is so low that the high-energy (>10 eV) tail population of photoelectrons become important (Harada et al., 2013; Pedersen, 1995), equivalent to a higher effective electron temperature that could lead to large (a few tens of Volts) positive surface potentials (Harada et al., 2017).

In addition to variable plasma conditions, the surface photoelectron current should vary substantially in response to solar photon flux variations associated with solar cycle, solar rotation, and transient solar flare events, which leads to significant variations in surface potentials as well (e.g., Farrell et al., 2013). Strong surface charging potentially causes dynamic charged dust transport (Poppe & Horányi, 2010; Sternovsky et al., 2008; Stubbs et al., 2006), modifies exospheric pickup ion dynamics (Poppe et al., 2013), and could be hazardous to human and robotic exploration (Farrell et al., 2008). Particularly, the solar X-ray flux is highly variable during solar flares (over an order of magnitude (e.g., Chamberlin et al., 2008)). This further raises the need for more accurate information on the higher energy extension of the yield function and photoelectron spectra, which may drastically change surface/dust charging during solar flares if the incident electron flux happens to be small (e.g., Sternovsky et al., 2008). Despite the need to accurately predict and assess the lunar electrostatic environment in all ambient plasma conditions that the Moon encounters, the existing charging models are limited to relatively high ambient electron flux cases (i.e., the solar wind), owing to the lack of information on the lunar surface photoemissivity for >20 eV photons.

In this study, we constrain the lunar surface photoemissivity over a wide energy range (~ 10 – 500 eV photons) with data from the Acceleration, Reconnection, Turbulence, and Electrodynamics of the Moon's Interaction with the Sun (ARTEMIS) mission combined with full solar irradiance spectra from Version 2 of the Flare Irradiance Spectral Model (FISM2) (Chamberlin et al., 2007, 2008, 2020). The ARTEMIS mission consists of two probes orbiting the Moon in elliptical orbits, P1 and P2 (originally probes B and C of the Time History of Events and Macroscale Interactions during Substorms (THEMIS) mission). Each probe carries a comprehensive suite of plasma and field instruments (Angelopoulos, 2011) and started collecting data in the lunar plasma environment in mid-2011. FISM2 is an empirical solar spectral irradiance model based on the Solar Radiation and Climate Experiment (SORCE) X-Ray Photometer System, the Solar Dynamics Observatory (SDO) Extreme ultraviolet Variability Experiment (EVE) and the SORCE Solar Stellar Irradiance Comparison Experiment. This observation-based empirical model provides solar irradiance estimations between 0.1 and 190 nm (i.e., 12.4 keV–6.5 eV) with 0.1 nm resolution and either daily or 60 s time cadence. We have selected four dates on which we can confidently identify lunar photoelectrons in the ARTEMIS ESA data, December 29, 2012 (in the magnetotail lobe), June 22, 23, and 25 2014 (in the solar wind), to investigate the lunar surface photoemission yields.

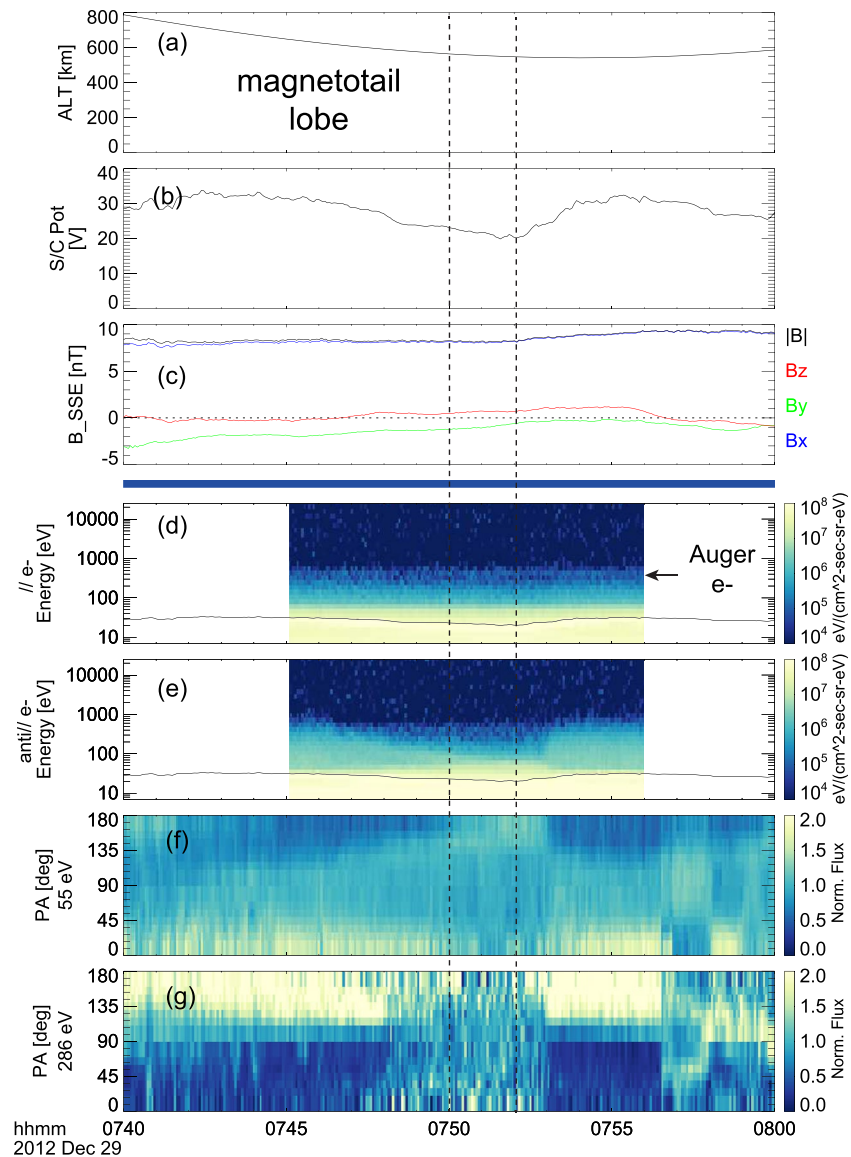


Figure 1. Acceleration, Reconnection, Turbulence, and Electrodynamics of the Moon's Interaction with the Sun (ARTEMIS) Probe 1 observations when the Moon was in Earth's magnetotail lobe on December 29, 2012. Time series of altitude (a), spacecraft potential (b), magnetic field vector in Solar-Selenocentric-Ecliptic (SSE) (c), (d) parallel (PA 0–10°) and (e) antiparallel (PA 170°–180°) electron differential energy fluxes (burst data product), pitch angle distributions for 55 eV (f) and 286 eV (g) (full data product). Electron data in panels (d–g) not yet corrected for spacecraft potentials. The blue bar between (c) and (d) shows magnetic connectivity to the lunar surface, using the straight line approximation. The spacecraft potential is also overplotted in panels (d) and (e). The two vertical dashed lines indicate the time range of electron energy spectra being obtained in Figures 3 and 4.

2. Photoelectron Observations: Example Cases

Harada et al. (2017) reported photoelectron observations by ARTEMIS Probe 1 when the Moon was in Earth's magnetotail lobe. It is worthwhile to re-examine this case study. The selected observations are displayed in Figure 1, including the magnetic field vectors measured by the fluxgate magnetometer (FGM) (Auster et al., 2008) and electron observations from the Electro-Static Analyzer (ESA) (McFadden et al., 2008). The magnetic field (panel c) is shown in the standard Solar-Selenocentric-Ecliptic (SSE) coordinate frame, where the X axis points from the center of the Moon to the Sun, the Z axis points to ecliptic north, and the Y axis completes the right-handed system. Panels (d) and (e) show electron energy spectra (burst data product, which provides the highest energy, angle, and time resolution available) separated for parallel (PA 0°–10°)

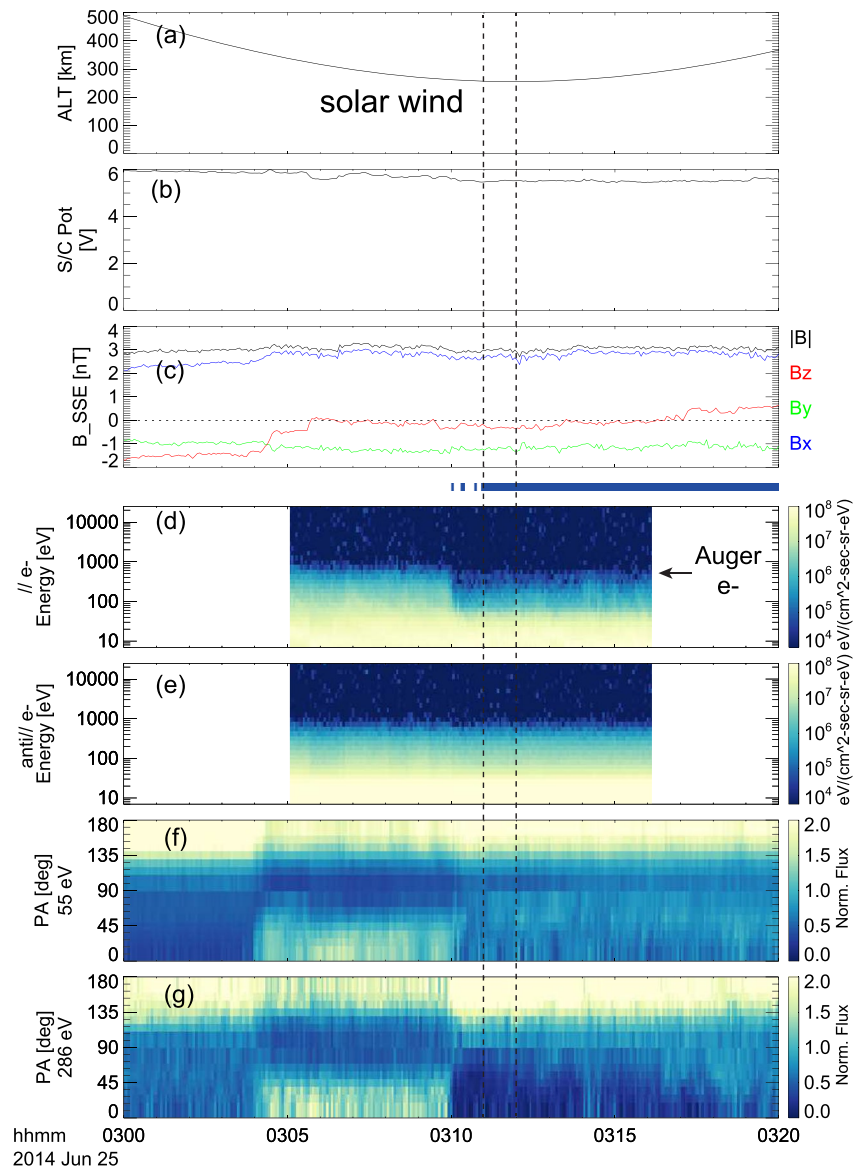


Figure 2. Time series of Acceleration, Reconnection, Turbulence, and Electrostatics of the Moon's Interaction with the Sun (ARTEMIS) Probe 1 observations when the Moon was in the solar wind on June 25, 2014, the same format as Figure 1.

and antiparallel (PA 170° – 180°) directions and panels (f and g) the pitch angle (PA) distributions for 55 and 286 eV (full data product), respectively. The burst data product provides a finer energy resolution and a higher time cadence than the full data product. Electron data in panels (d–g) are not yet corrected for the spacecraft potential (U_{sc}), which is provided in panel (b). The spacecraft potential is measured by the ARTEMIS probes and provided and publicly available as part of the standard data product (Bonnell et al., 2009).

In Figure 1d, a distinctive high-flux line at an energy of 400–500 eV in the electron energy spectra is observed from $\sim 07:45$ to $\sim 07:56$ UT (universal time), which coincides with the theoretical energy of oxygen Auger electrons (Lin & Gopalan, 1991; Mitchell et al., 2000; Willis et al., 1973; Xu et al., 2018, 2019). Auger electrons are produced when solar X-ray photons are energetic enough to eject an inner shell electron. The resultant ion then relaxes via emitting a fluorescence X-ray or ejecting another outer shell electron carrying the excess energy, both of which have a precise energy determined by the energy difference between the two states. These emitted electrons with a fixed energy are called Auger electrons, around 500 eV for the oxygen

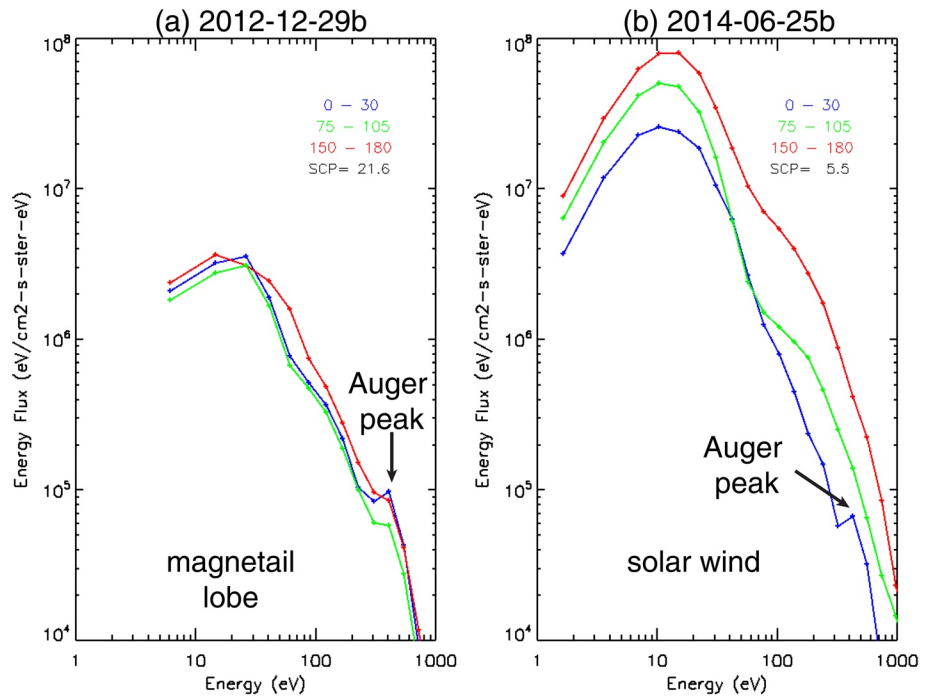


Figure 3. Energy spectra for PA 0–30°, 75°–105°, and 150°–180° in the magnetotail lobe (a) and solar wind (b), only corrected for spacecraft potentials (U_{sc}). Electron energy spectra in (a and b) are averaged over the time intervals indicated by the two vertical lines in Figures 1 and 2, respectively.

atom, which is one of the most abundant atomic constituents on the lunar surface. In the anti-parallel direction, such a feature can be identified, albeit less clear, in panel (e) from ~07:48 to ~07:53 UT, presumably due to reflection at a distant mirror point. This is the first report of Auger electron observations at the Moon (to our best knowledge) by the ARTEMIS spacecraft. This provides a unique feature to unambiguously identify photoelectrons emitted from the lunar surface. Indeed, throughout the displayed orbit segment in Figure 1, the magnetic field line can be traced back to the lunar surface with a straight line approximation (the blue bar between panels b and c). With $B_{XSSSE} > 0$ and the ARTEMIS spacecraft located on the Sun-side of the Moon, parallel electrons would be photoelectrons streaming away from the Moon.

We also identify photoelectron observations when the Moon is in the solar wind (June 25, 2014), as shown in Figure 2 with the same format as Figure 1. Similarly, with $B_{XSSSE} > 0$ and ARTEMIS located on the Sun-side of the Moon, Auger electrons can be identified in the parallel direction from 03:10 to 03:16 UT in panel (d), corresponding to a magnetic connectivity to the lunar surface. In contrast, anti-parallel electrons consist of incident solar wind electrons. In Figures 2f and 2g, from 03:04 to 03:10 UT, the magnetic field line is likely unconnected to the Moon even though a bi-directional pitch angle distribution is observed, probably caused by a connectivity to Earth's bow shock.

To illustrate more clearly the spectral features of lunar photoelectrons and how they differ from other electron populations, Figure 3 displays the energy spectra separated for parallel, perpendicular, and anti-parallel directions, averaged over the time intervals indicated by the two vertical lines in Figures 1 and 2, both now corrected for spacecraft potentials. The standard procedure to correct for a (spacecraft or lunar) potential effect (U) is to first convert the measured electron number flux, $f(\epsilon)$, to phase space densities, which are then shifted in energy by eU and lastly converted back to fluxes. For a given electron energy ϵ , the corrected electron number flux f' would be $f'(\epsilon') = f(\epsilon) \frac{\epsilon - eU}{\epsilon}$ at a new energy of $\epsilon' = \epsilon - eU$. When $\epsilon' < 0$ or $\epsilon < eU$, electrons would be repelled by this potential and could not be measured by the spacecraft. In Figure 3a, when ARTEMIS was in the magnetotail lobe, the blue spectrum is upgoing electrons, with a distinctive Auger peak at ~500 eV, indicating these electrons are escaping lunar surface photoelectrons with initial energies surpassing the lunar surface potential.

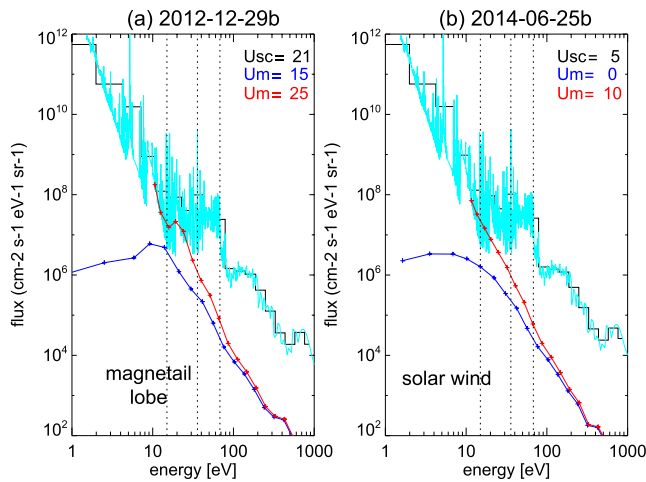


Figure 4. The blue and red lines are energy spectra of electrons traveling away from the Moon (PA 0–30° as $B_{\text{SSSE}} > 0$ and the spacecraft located on the dayside), corrected for assumed low and high lunar surface potentials (U_m), as well as spacecraft potentials (U_{sc}). The cyan lines are solar photon fluxes from Version 2 of the Flare Irradiance Spectral Model (FISM2) in its original resolution (converted to energy from 0.1 nm bins) and the black lines with an energy resolution comparable to the electron energy resolution. (a) for December 29, 2012 and (b) for June 25, 2014. Electron energy spectra in (a and b) are averaged over the time intervals indicated by the two vertical lines in Figures 1 and 2, respectively.

Anderson & Lin, 1969; Lin, 1968; McCoy et al., 1975). Lastly, the high fluxes in the antiparallel direction might be caused by a mixture with another electron population. Regardless of the possible magnetic topology, Figure 3a provides a clean example for the lunar photoelectron spectrum, particularly the blue spectrum.

Figure 3b shows the spectra for when ARTEMIS was in the solar wind, also corrected for spacecraft potentials (U_{sc}). Similarly, in the parallel direction, the overall flux is significantly lower than incoming solar wind electrons (red, antiparallel) with the distinctive Auger electron peak at 500 eV. We interpret this as

evidence of field-line connection to the lunar dayside on one end and to the undisturbed solar wind on the other end. Photoelectron fluxes (blue) in Figure 3a are significantly lower than that in Figure 3b because the lunar dayside surface potential is higher in the lobe, which not only traps a greater fraction of the emitted photoelectrons near the surface but also decelerates escaping electrons. The lunar surface potential (U_m) in the magnetotail lobe case is determined to be 15–25 V by Harada et al. (2017) with ion reflectometry (an energy-dependent loss cone in the ion distribution) while U_m is usually between 0 and 10 V in the solar wind (e.g., Freeman & Ibrahim, 1975; Manka & Michel, 1973; Poppe & Horányi, 2010). However, as pointed out by Harada et al. (2017), ion reflectometry is not always available such that the dayside surface potential is hard to determine while in the magnetotail lobes. Meanwhile, the correction to this relatively large surface potential in the magnetotail lobe cannot be neglected. In contrast, when the Moon is immersed in the solar wind, the dayside surface potential is relatively small and can be approximated well with an upper and lower bound of 0 and 10 V. Therefore, in this study, we take two more examples, June 22–23, 2014, when the Moon is in the solar wind and we confidently identify as lunar photoelectron observations to conduct a semi-statistical analysis. The photoelectron energy spectra and

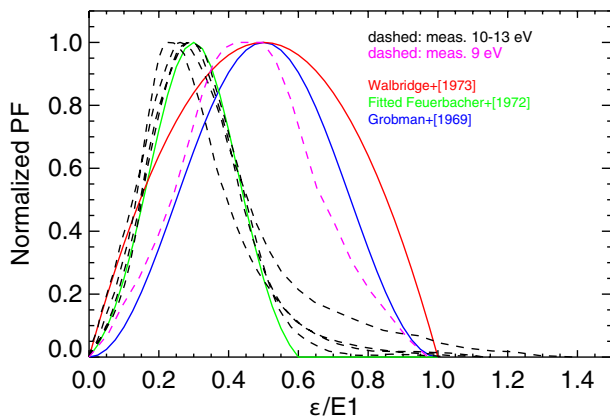


Figure 5. Probability functions (PFs) from literature normalized by the peak probability. The black and magenta dashed lines are experiment results from Feuerbacher et al. (1972). The green, blue, and red solid lines are approximated formulas for PFs used in this study.

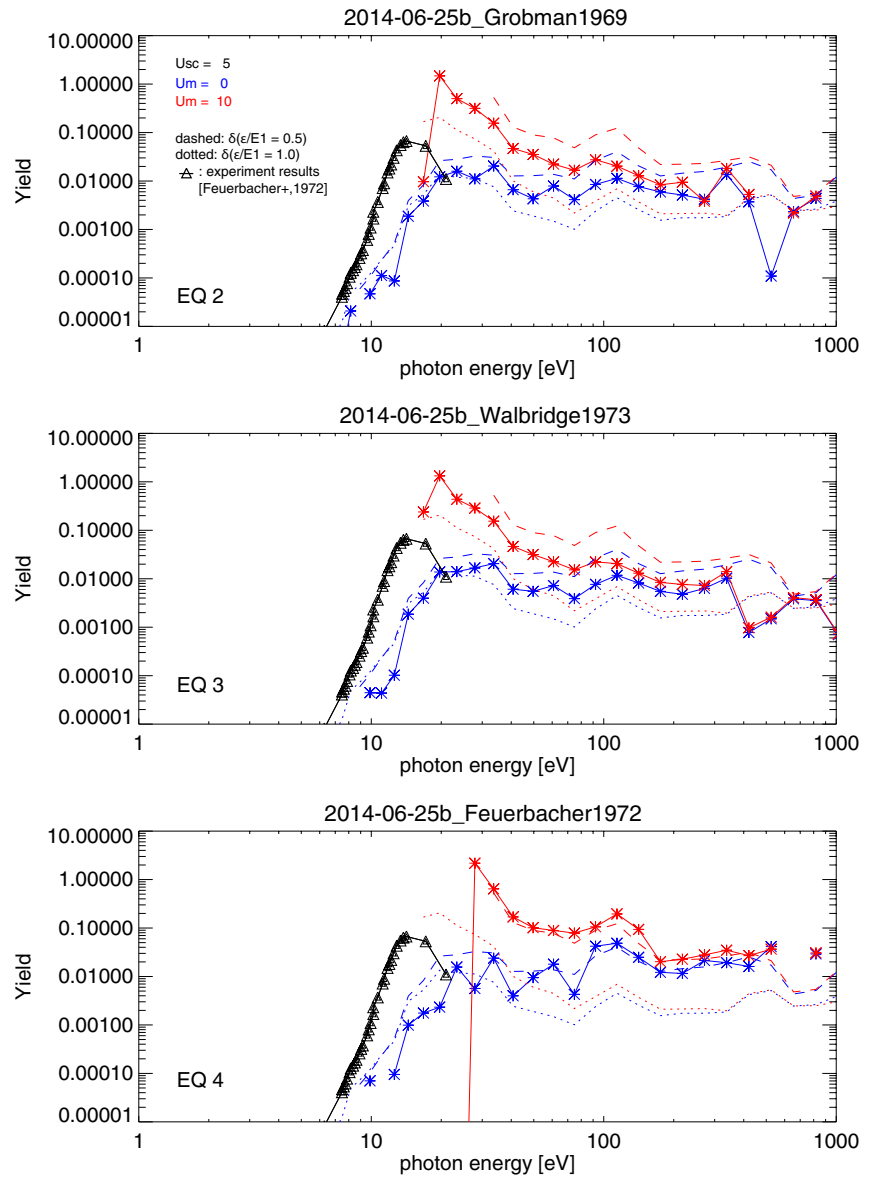


Figure 6. Calculated yield based on different Probability functions (PFs). Dotted and dashed lines are for delta functions $\delta(\epsilon/E_1)$ with $\epsilon/E_1 = 1$ and $\epsilon/E_1 = 0.5$, respectively. Solid lines for Equations 2–4: (a) from Equation 2 (Grobman & Blank, 1969), (b) from Equation 3 (Reasoner & Burke, 1972; Walbridge, 1973), and (c) from Equation 4 (Feuerbacher et al., 1972). The blue and red lines are for low and high U_m , respectively. Black triangles are yields from experiments by Feuerbacher et al. (1972).

solar photon spectra for these two days are very similar to that for June 25, 2014 such that we include these spectra only in the supplementary material (Figures S1 and S2).

3. Photoemission Yields

3.1. Theoretical Background

In general, the photoelectron flux emitted from the lunar surface, $f(\epsilon)$, as a function of photoelectron energy, ϵ , is given by,

$$f(\epsilon) d\epsilon = \int_W^\infty S(E)Y(E)F(\epsilon, E) dE d\epsilon \quad (1)$$

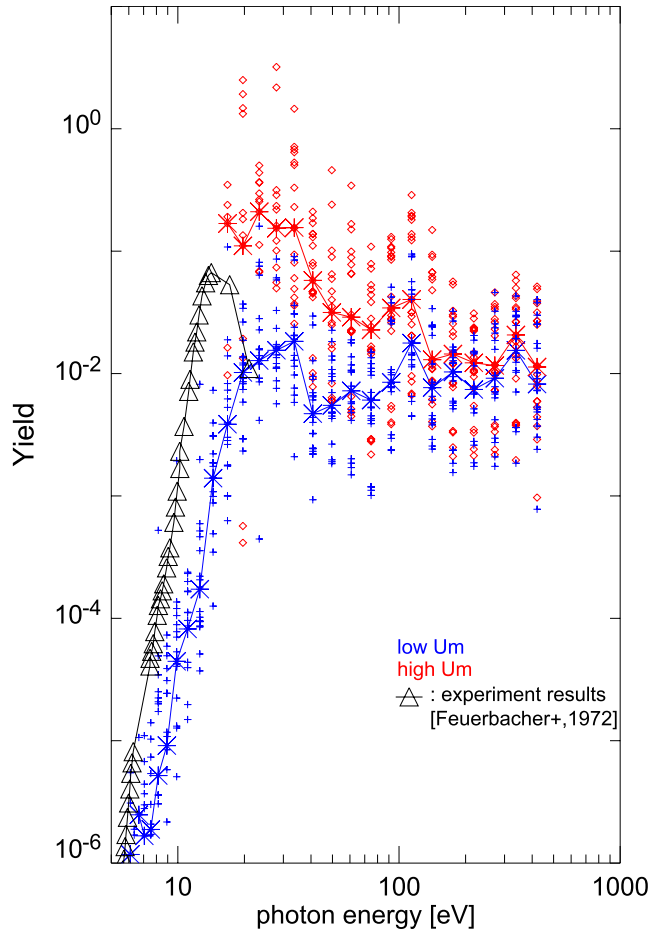


Figure 7. Calculated yields for five Probability functions (PFs) in total, three based on Equations 2–4 and two delta functions, $\delta(\epsilon/E_1 = 0.5)$ and $\delta(\epsilon/E_1 = 1)$, for all four selected dates. Red and blue indicate assumed low and high lunar surface potentials (U_m) and solid lines are median values. Again, black triangles are yields from experiments by Feuerbacher et al. (1972) as a comparison.

from the lunar surface to the spacecraft to be nonmonotonic, which typically only occurs when the lunar surface potential is negative with respect to the spacecraft (e.g., Poppe et al., 2011), as opposed to the cases studied here where the lunar surface potential is positive with respect to the spacecraft. With corrections for both U_{sc} and U_m , the photoelectron fluxes for different dates are very similar, just as the solar photon fluxes happen to be similar for the selected dates. As the photoelectron spectrum obtained in the magnetotail lobe is unlikely contaminated by other populations, a similar electron distribution in Figure 3b implies that any secondary electrons produced by incident solar wind electrons are likely lower in flux than lunar photoelectrons.

Another key piece required to solve Y is the probability function, $F(\epsilon, E)$. While Feuerbacher et al. (1972) provides laboratory measurements of F for photon energies $E < 20$ eV, it is very poorly constrained at higher photon energies ($E > 20$ eV). Past literature has formulated F with general assumptions including $F = 0$ at an electron energy of $\epsilon = 0$ and $\epsilon \geq E_1$ with a width comparable to E_1 . Two representative formulas from previous literature include:

$$F = A_0 \sin(\pi \epsilon / E_1)^2 / E_1; \text{ (Grobman \& Blank, 1969);} \quad (2)$$

where W is the work function of the material, $S(E)$ is the solar flux as a function of photon energy $E = h\nu$, and $Y(E)$ is the yield function. $F(\epsilon, E)$ is the photoelectron probability function, which represents the normalized photoelectron energy distribution for monochromatic light incidence ($\int_0^\infty F(\epsilon, E) d\epsilon = 1$).

Discretizing Equation 1 over ϵ and E yields a matrix equation, $f_i = \sum_j S_j Y_j F_{ij} dE_j$, where f_i is the i_{th} element of the photoelectron measurements ($i = 1, 2, \dots, n$) and Y_j is the j_{th} element of the discretized yield function ($j = 1, 2, \dots, m$). Defining an $n \times m$ matrix \mathbf{A} as $A_{ij} = S_j F_{ij} dE_j$, we obtain a vectorized expression, $f = \mathbf{A}Y$. By specifying a probability function, F_{ij} , determining Y from the measurements of f corresponds to solving a matrix inversion problem, $Y = \mathbf{A}^{-1}f$.

3.2. Inputs

To derive yields, Y , we take photoelectron fluxes ($f(\epsilon)$) measured by ARTEMIS and corresponding solar irradiance spectra (S) from FISM2 as inputs. Figure 4 shows the photoelectron energy spectra (i.e., parallel electrons in Figure 3) corrected for U_{sc} and assumed high (red) and low (blue) lunar surface potentials (U_m). Note that, even though both U_{sc} and U_m are positive, photoelectrons produced at the lunar surface would first be decelerated by the positive U_m and then accelerated by the positive U_{sc} before being measured by the ESA instrument. The correction to both potentials is to reverse this two-stage process and some of the low energies are not available because these electrons are returned and trapped within the surface sheath by U_m . The solar photon fluxes from FISM2 are also overlaid, converted to available photon energy (E_1), in its original 0.1-nm resolution (cyan) and in an energy resolution comparable to the electron energy resolution (black). For a direct comparison between photoelectron fluxes and solar photon fluxes, we calculate an available photon energy $E_1 = E - W$, where $W = 5$ eV from Feuerbacher et al. (1972) is used. Note that the electron burst data product from ARTEMIS has a $\Delta\epsilon/\epsilon \sim 32\%$, i.e., $\Delta\epsilon > 6$ eV for electron energies > 20 eV, such that the $\sim 1\text{--}2$ eV uncertainty in W should not significantly impact our results. For the case on December 29, 2012, a range of $U_m = [15, 25]$ V is used, determined by Harada et al. (2017), while for the cases (June 22, 23, and 25 2014) when the Moon is immersed in the solar wind, a range of $U_m = [0, 10]$ V is assumed. We also do not expect the potential profile

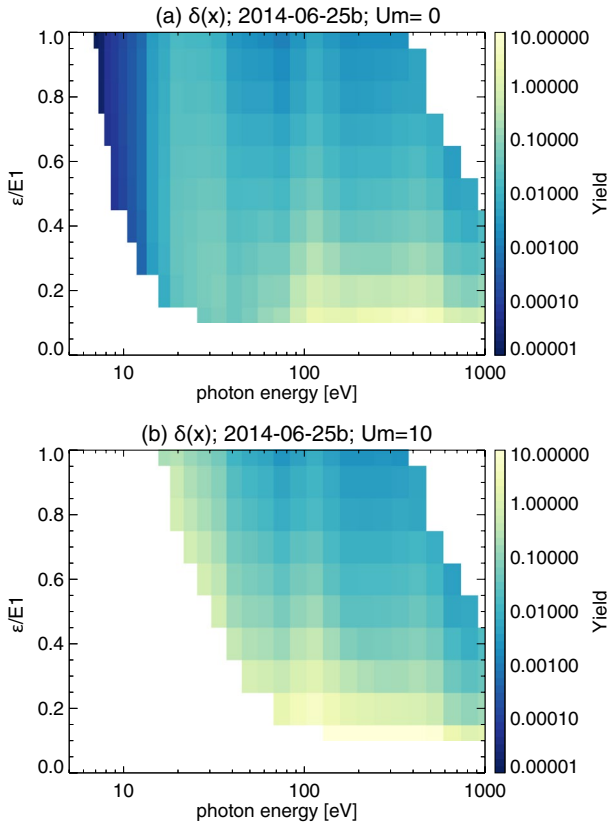


Figure 8. Calculated yields for June 25, 2014 with $\delta(x)$ as Probability functions (PFs) as a function of photon energy E and x , where $x = \epsilon/E_1$. Panels (a and b) are for $U_m = 0$ and $U_m = 10$ V, respectively.

$$F = A_1 \epsilon * (E_1 - \epsilon) / E_1^3; (\text{Reasoner \& Burke, 1972; Walbridge, 1973}) \quad (3)$$

where A_0 and A_1 are normalization factors to satisfy $\int_0^\infty F(\epsilon, E) d\epsilon = 1$. These two probability functions (PFs) are shown in Figure 5 as the blue and red lines, respectively, with the peak probability normalized to 1 for a better comparison. Both functions peak at $\epsilon/E_1 = 0.5$. Meanwhile, experimental results from Feuerbacher et al. (1972), also overlaid in Figure 5, display a peak of F at $\epsilon/E_1 = \sim 0.3$ for discrete photon energies between 10 and 13 eV (black dashed lines) and $\epsilon/E_1 = \sim 0.45$ for 9 eV photons (magenta dashed line). We can approximate the experimental results with the following equation:

$$F = A_2 \left[\exp \left(- \left(\frac{0.3 - (\epsilon / E_1)}{0.182} \right)^2 \right) - \exp \left(- \left(\frac{0.3}{0.182} \right)^2 \right) \right] \quad (4)$$

where A_2 is again a normalization factor to ensure the integral over electron energy is unity. The second term in Equation 4 is to ensure $F = 0$ at $\epsilon = 0$, shown as the green line in Figure 5.

Lastly, the simplest PF is a delta function $\delta(\epsilon/E_1)$, which represents a photon with an available energy E_1 that solely produces photoelectrons with an energy of ϵ . A delta function is not physically realistic but it avoids the complication of solving matrix inversions while providing a method for gaining simple physical insight. We will also show later that results from other PFs can be reasonably well approximated by delta functions.

3.3. Deriving Yields

In this study, we take Equations 2–4 as PFs and apply to all photon energies to derive yields. While it is very likely that PFs differ significantly for different photon energies, it is our intention to illustrate the large uncertainty in yields even with these simplified PFs. We derive yields with a standard matrix inversion procedure, singular value decomposition, to solve the linear least squares problem. The resultant yields for June 25, 2014 are shown in Figure 6 for the three PFs based on Equations 2–4. Results for yields from delta functions with $\epsilon/E_1 = 1$ and $\epsilon/E_1 = 0.5$ are also displayed as dotted and dashed lines. In the same figure, we overlay yields for photon energies $E < 20$ eV from experiments by Feuerbacher et al. (1972) for comparison.

A few observations can be made for this case study. In Figure 6, there are several similar behaviors shared across the various PFs: (1) The derived yields remain relatively constant for photon energies 50–500 eV, as opposed to falling rapidly with increasing energy. This is because photon fluxes and electron fluxes have similar slopes at this energy range (Figure 3) and each assumed PF is similar for different photon energies and peaks at the same ratio of ϵ/E_1 . (2) There is a peak near 100 eV in all calculated yields, which comes from the large photon flux change near 70 eV (Figure 3). More specifically, to produce the same level of electron fluxes, a higher yield is required if the source photon flux is lower. Because of the relatively coarse photon and electron energy resolution used to calculate the yield, the first energy bin with a much lower photon flux, past this photon flux drop-off at 70 eV, is ~ 100 eV, leading to the peak in yield at a similar energy. (3) The solutions at the two bounding surface potential values (blue and red lines) differ more at low energies, as expected. (4) The inferred yield past the Auger electron peak (~ 500 eV) might not be accurate. While valence photoelectrons and Auger electrons have the same source, that is photoemission by solar photons, the process of liberating an electron at the atomic level is different such that the application of the work function via the simple relation $E_1 = E - W$ for valence photoelectrons is not suitable for Auger electrons (Lin & Gopalan, 1991; Willis et al., 1973).

A few observations can be made for this case study. In Figure 6, there are several similar behaviors shared across the various PFs: (1) The derived yields remain relatively constant for photon energies 50–500 eV, as opposed to falling rapidly with increasing energy. This is because photon fluxes and electron fluxes have similar slopes at this energy range (Figure 3) and each assumed PF is similar for different photon energies and peaks at the same ratio of ϵ/E_1 . (2) There is a peak near 100 eV in all calculated yields, which comes from the large photon flux change near 70 eV (Figure 3). More specifically, to produce the same level of electron fluxes, a higher yield is required if the source photon flux is lower. Because of the relatively coarse photon and electron energy resolution used to calculate the yield, the first energy bin with a much lower photon flux, past this photon flux drop-off at 70 eV, is ~ 100 eV, leading to the peak in yield at a similar energy. (3) The solutions at the two bounding surface potential values (blue and red lines) differ more at low energies, as expected. (4) The inferred yield past the Auger electron peak (~ 500 eV) might not be accurate. While valence photoelectrons and Auger electrons have the same source, that is photoemission by solar photons, the process of liberating an electron at the atomic level is different such that the application of the work function via the simple relation $E_1 = E - W$ for valence photoelectrons is not suitable for Auger electrons (Lin & Gopalan, 1991; Willis et al., 1973).

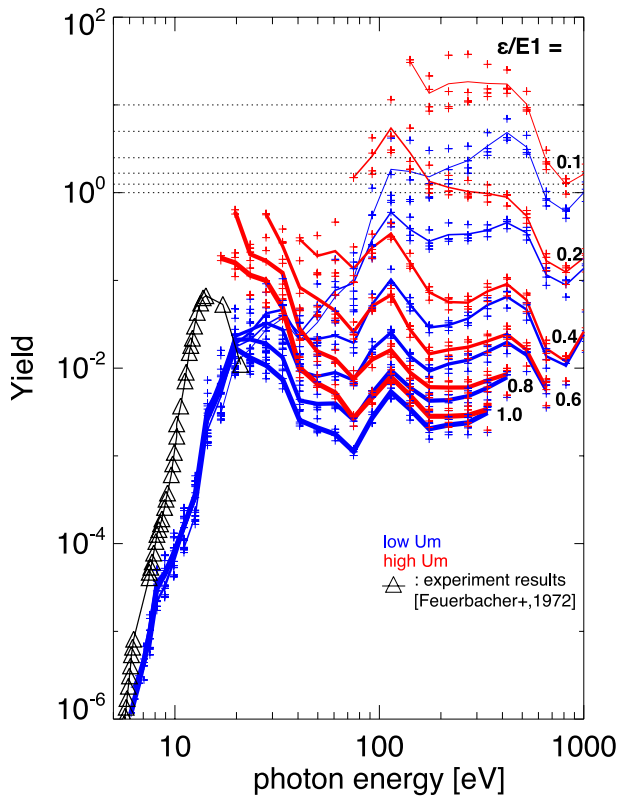


Figure 9. Median yields for all four days ('+') with delta functions $\delta(x)$ as Probability functions (PFs) for different/selected $x = \epsilon/E_1$. Median values are shown as blue and red lines, separated for assumed low and high lunar surface potentials (U_m). Black triangles are yields from experiments by Feuerbacher et al. (1972) as a comparison.

Meanwhile, differences exist between the different PFs. Results with Equation 2 (panel a) and Equation 3 (panel b) are similar as these two equations share similar shapes while yields are generally higher from Equation 4 (panel c). This is because the PF from Equation 4 peaks at a lower $\epsilon/E_1 \sim 0.3$, in comparison to $\epsilon/E_1 \sim 0.5$ for the other two PFs. Lastly, we show the yields determined with delta functions as a comparison to other PFs, that is the dotted and dashed lines in Figure 6. Yields inferred from Equations 2 and 3 can be relatively well-approximated with a delta function $\delta(\epsilon/E_1 \sim 0.7)$ for photon energies >20 – 30 eV, in contrast to an equivalent delta function $\delta(\epsilon/E_1 \sim 0.5)$ for Equation 4 (panel c), corresponding to a lower peak ratio of ϵ/E_1 in PF.

Figure 7 displays the inferred yields from five PFs, three based on Equations 2–4 and two delta functions, $\delta(\epsilon/E_1 = 0.5)$ and $\delta(\epsilon/E_1 = 1)$, for all four selected dates, separated for assumed low (blue) and high (red) U_m . Yields mostly range from 0.001 to 1 for photon energies above 20 eV. As indicated by the solid red and blue lines in Figure 7, we find a median yield on the order of ~ 0.01 for photon energies $E \sim 50$ – 500 eV, although with at least an order-of-magnitude scattering/uncertainty. For photon energies $E < 30$ eV, the experimental results from Feuerbacher et al. (1972) (black triangles) are bracketed by our derived yields and a good agreement can be achieved with a certain U_m within the assumed potential range.

3.4. Sensitivity Study of Photoemission Yields

Figure 7 seemingly suggests we can derive yields within a reasonable uncertainty (to within an order of magnitude), but this is largely because our PFs have similar assumptions, such as peaking at a similar ratio of ϵ/E_1 . In reality, there is no experimental result (to our best knowledge) to evaluate the plausibility of these PFs for photon energies above 20 eV. We therefore conduct a sensitivity study with delta functions $\delta(\epsilon/E_1)$ at different ϵ/E_1 , as the resulting yields from Equations 2–4 can be reasonably well approximated with these delta functions.

Figure 8 illustrates the derived yields for June 25, 2014 with $\delta(x)$ as PFs as a function of photon energy E and x , for $U_m = 0$ (panel a) and $U_m = 10$ V (panel b), where $x = \epsilon/E_1$. As photon fluxes generally decrease with increasing energies (or shorter wavelengths), the resulting yield increases with a decreasing x . In other words, we can infer a lower bound for yields with $x = 1$ (i.e., the specific case in which photoelectrons are emitted with the full energy available from the incoming photon minus the work function). The resulting yields have different energy ranges at different x because we impose a maximum electron energy of 420 eV (below the Auger peak) for this calculation (recall that the Auger process makes the calculation with a work function of 5 eV inappropriate). The peak in yield at a photon energy ~ 100 eV is caused by the large photon flux change near ~ 70 eV (Figure 4), as explained above. Conversely, the drop-off in yield past ~ 600 eV is caused by the photon flux enhancement at 600–800 eV (Figure 4).

Figure 9 summarizes the results of this sensitivity study for all four days ('+') with with delta functions $\delta(x)$ as PFs for different/selected $x = \epsilon/E_1$. The results from these four selected dates show a small variation, of a factor of a few, implying our successful selection of photoelectron measurements. As mentioned above, yields based on $\delta(\epsilon/E_1 = 1)$ can be taken as a lower bound, which gives 10^{-3} for photon energies above ~ 20 eV, instead of falling off exponentially with increasing energies. The more-or-less converging yield for photon energies below 20 eV with $U_m = 0$ V (blue lines and '+') is because the electron fluxes remain roughly the same within this energy range (Figure 4). Meanwhile, depending on x , the derived yield for high energies can vary by ~ 4 orders of magnitude, which provides motivation for future studies to better constrain the photoelectron energy probability function for high energies.

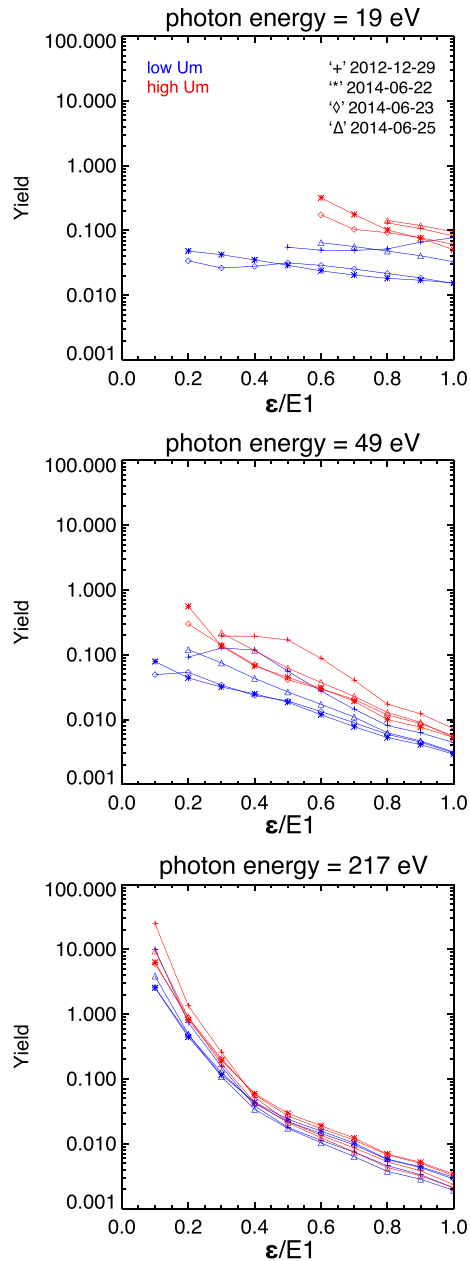


Figure 10. Derived yields based on $\delta(x)$ as a function of x for assumed low (blue lines) and high (red lines) U_m for four selected cases (different symbols, '+' for 2012-12-29, '*' for 2014-06-22, '◊' for 2014-06-23, and 'Δ' for 2014-06-25). From the top to bottom are for three selected photon energies of 19, 49, and 217 eV.

function $\delta(x)$ as a function of x , separated for assumed low (blue lines) and high (red lines) U_m , for the four selected observations on different days (different symbols). As shown in Figure 10, the inferred yield overall differs by a factor of 2–3 for different days. As expected, the uncertainty in U_m causes a larger uncertainty in yields for low-energy photons, a factor of ~ 2 –3 for 19-eV and 49-eV photons, but is a negligible effect for 217-eV photons. In contrast, different x values impart an uncertainty of a factor of few in yield for 19-eV photons, about two orders of magnitude for 49-eV photons, and nearly four orders of magnitude for 217-eV photons. In other words, the uncertainty caused by an unknown PF, here represented by $\delta(x)$ with different

4. Discussion and Conclusions

In this study, we have identified photoelectrons emitted from the lunar surface in both Earth's magnetotail lobe and the solar wind via the Auger electron peak. This is the first report of Auger electron observations at the Moon (to our best knowledge) by the ARTEMIS spacecraft, which provides a unique feature to identify photoelectrons emitted from the lunar surface. Combined with solar irradiance spectra from FISM2, we have constrained the photoemission yield over a wide photon energy range, from <10 to ~ 500 eV. However, this is achieved with considerable assumptions on the PF, which is not well constrained beyond ~ 20 eV. We also neglected the effect of the incidence angle of solar photons for simplicity, to which the correction is probably unimportant considering the large uncertainty in the inferred yields.

More specifically, we applied two PFs used in the literature (Grobman & Blank, 1969; Reasoner & Burke, 1972; Walbridge, 1973) over the entire energy range and also generalized the PF based on low-energy experiment results (Feuerbacher et al., 1972) to above 20 eV. The resulting yields share similarities, such as a relatively constant value (on the order of 0.01) for photon energies ~ 50 –500 eV because of a similar slope in electron fluxes and photon fluxes against energy, and a local peak at a photon energy of ~ 100 eV because of a large photon flux change near 70 eV. We also find that these results can be approximated relatively well with a PF in the form of a delta function $\delta(x)$, where x is the ratio of the electron's kinetic energy ϵ and the photon's available energy E_1 .

Our derived yields from these PFs (Equations 2–4) are constrained within a reasonable uncertainty (to within an order of magnitude). However, this is because these PFs are very similar with assumptions such as peaking at a fixed $x = \epsilon/E_1$ for different photon energies. This motivates us to conduct a sensitivity study with delta functions $\delta(x)$ at different x . Results based on $\delta(\epsilon/E_1 = 1)$ provide a lower bound for the yield, as photon fluxes generally decrease with increasing energies. This gives a lower bound of 10^{-3} for photon energies above ~ 20 eV, instead of falling off exponentially with increasing energies. Reasoner and Burke (1972) calculated a photoelectron yield of 0.1, assumed to be constant for photon energies >9 eV. Experimental results also give a yield close to 0.1 for metals for photon energies of ~ 100 –1,000 eV (e.g., Cimino & Schäfers, 2014; Day et al., 1981). If we assume 0.1 to be the upper limit of the photoemission yield for photon energies $>\sim 100$ eV, then $x = \epsilon/E_1 > \sim 0.4$ when we use the delta function as the PF.

Our sensitivity study also reveals an uncertainty over ~ 4 orders of magnitude in yield for photon energies $>\sim 30$ eV with different x values assumed. To further analyze the possible causes of the uncertainty in yield, we select three photon energies to be representative of the entire energy range, 19, 49, and 217 eV, and show the derived yields based on the delta

x values, is the main cause of large uncertainties in yield for photons on the order of $>$ a few tens eV, while the uncertainty in U_m is a significant contributor as well for low-energy ($<$ a few tens eV) photons.

In summary, the photoemission yield is one of the fundamental properties of solid materials, but not yet determined for photon energies above ~ 20 eV for the lunar surface. We have constrained this yield with a combination of data from the ARTEMIS mission and the solar irradiance spectra from FISM2. While we infer a lower bound of 10^{-3} in yield for photon energies $>\sim 20$ eV, we find an uncertainty over ~ 4 orders of magnitude in derived yields, owing to a poorly constrained probability function, which motivates future experiments on lunar samples to better characterize the lunar surface charging environment.

Data Availability Statement

All ARTEMIS data necessary for this study are publicly available at <http://artemis.ssl.berkeley.edu>. The FISM2 data is publicly available at <http://lasp.colorado.edu/lisird/fism>. Data access and processing was done using SPEDAS V3.1, see Angelopoulos et al. (2019)

Acknowledgments

S. Xu, A.R. Poppe, and J.S. Halekas gratefully acknowledge support from NASA's Solar System Exploration Research Virtual Institute (SSERV), grants #NNX14AG16A and #NNX-15AH15A. A.R. Poppe and S. Xu also acknowledge support from NASA's Lunar Data Analysis Program, grant #80NSSC18K1565. The ARTEMIS mission is funded and operated under NASA grant NAS5-02099, and we specifically acknowledge K.-H. Glassmeier, U. Auster, and W. Baumjohann for the use of FGM data provided under the lead of the Technical University of Braunschweig and with financial support through the German Ministry for Economy and Technology and the German Center for Aviation and Space (DLR), contract 50 OC 0302.

References

Anderson, K., & Lin, R. P. (1969). Observation of interplanetary field lines in the magnetotail. *Journal of Geophysical Research*, 74(16), 3953–3968. <https://doi.org/10.1029/ja074i016p03953>

Angelopoulos, V. (2011). The ARTEMIS Mission. *Space Science Reviews*, 165, 3–25. <https://doi.org/10.1007/s11214-010-9687-2>

Angelopoulos, V., Cruce, P., Drozdov, A., Grimes, E., Hatzigeorgiu, N., King, D., et al. (2019). The Space Physics Environment Data Analysis System (SPEDAS). *Space Science Reviews*, 215(1), 9.

Auster, H., Glassmeier, K., Magnes, W., Aydogar, O., Baumjohann, W., Constantinescu, D., et al. (2008). The THEMIS fluxgate magnetometer. *Space Science Reviews*, 141(1–4), 235–264. <https://doi.org/10.1007/s11214-008-9365-9>

Bonnell, J., Mozer, F., Delory, G., Hull, A., Ergun, R., Cully, C., et al. (2009). The electric field instrument (EFI) for THEMIS. In *The THEMIS mission* (pp. 303–341). Springer. https://doi.org/10.1007/978-0-387-89820-9_14

Chamberlin, P. C., Eparvier, F. G., Knoer, V., Leise, H., Pankratz, A., Snow, M., et al. (2020). The flare irradiance spectral model-Version 2 (FISM2). *Space Weather*, 18, e2020SW002588. <https://doi.org/10.1029/2020SW002588>

Chamberlin, P. C., Woods, T. N., & Eparvier, F. G. (2007). Flare irradiance spectral model (FISM): Daily component algorithms and results. *Space Weather*, 5(7), 1–23. <https://doi.org/10.1029/2007sw000316>

Chamberlin, P. C., Woods, T. N., & Eparvier, F. G. (2008). Flare irradiance spectral model (FISM): Flare component algorithms and results. *Space Weather*, 6(5). <https://doi.org/10.1029/2007sw000372>

Cimino, R., & Schäfers, F. (2014). *Soft X-ray reflectivity and photoelectron yield of technical materials: Experimental input for instability simulations in high intensity accelerators*. WEPME034 (p. 3). CERN. <https://doi.org/10.18429/JACoW-IPAC2014-WEPME034>

Day, R. H., Lee, P., Saloman, E. B., & Nagel, D. J. (1981). Photoelectric quantum efficiencies and filter window absorption coefficients from 20 eV to 10 keV. *Journal of Applied Physics*, 52(11), 6965–6973. <https://doi.org/10.1063/1.328653>

Dove, A., Horányi, M., Robertson, S., & Wang, X. (2018). Laboratory investigation of the effect of surface roughness on photoemission from surfaces in space. *Planetary and Space Science*, 156, 92–95. <https://doi.org/10.1016/j.pss.2017.10.014>

Farrell, W., Poppe, A., Zimmerman, M., Halekas, J., Delory, G., & Killen, R. (2013). The lunar photoelectron sheath: A change in trapping efficiency during a solar storm. *Journal of Geophysical Research: Planets*, 118, 1114–1122. <https://doi.org/10.1002/jgre.20086>

Farrell, W., Stubbs, T., Delory, G., Vondrak, R., Collier, M., Halekas, J., & Lin, R. (2008). Concerning the dissipation of electrically charged objects in the shadowed lunar polar regions. *Geophysical Research Letters*, 35, L19104. <https://doi.org/10.1029/2008gl034785>

Feuerbacher, B., Anderegg, M., Fitton, B., Laude, L., Willis, R., & Grand, R. (1972). Photoemission from lunar surface fines and the lunar photoelectron sheath. In *Lunar and planetary science conference proceedings*, 3, (p. 2655).

Freeman, J., & Ibrahim, M. (1975). Lunar electric fields, surface potential and associated plasma sheaths. *The Moon*, 14(1), 103–114. <https://doi.org/10.1007/bf00562976>

Freeman, J., Jr, Fenner, M., & Hills, H. (1973). Electric potential of the moon in the solar wind. *Journal of Geophysical Research*, 78(22), 4560–4567. <https://doi.org/10.1029/ja078i022p04560>

Grand, R. (1997). Photoemission on the surface of mercury and related electrical phenomena. *Planetary and Space Science*, 45(1), 67–72. [https://doi.org/10.1016/s0032-0633\(96\)00096-7](https://doi.org/10.1016/s0032-0633(96)00096-7)

Grand, R. J. L., & Tunaley, J. K. E. (1971). Photoelectron sheath near a planar probe in interplanetary space. *Journal of Geophysical Research*, 76(10), 2498–2505. <https://doi.org/10.1029/JA076i010p02498>

Grobman, W., & Blank, J. (1969). Electrostatic potential distribution of the sunlit lunar surface. *Journal of Geophysical Research*, 74(16), 3943–3951. <https://doi.org/10.1029/ja074i016p03943>

Halekas, J., Delory, G., Farrell, W., Angelopoulos, V., McFadden, J., Bonnell, J., et al. (2011). First remote measurements of lunar surface charging from artemis: Evidence for nonmonotonic sheath potentials above the dayside surface. *Journal of Geophysical Research*, 116, A07103. <https://doi.org/10.1029/2011ja016542>

Halekas, J., Delory, G., Lin, R., Stubbs, T., & Farrell, W. (2008). Lunar Prospector observations of the electrostatic potential of the lunar surface and its response to incident currents. *Journal of Geophysical Research*, 113, A09102. <https://doi.org/10.1029/2008ja013194>

Halekas, J., Delory, G., Lin, R., Stubbs, T., & Farrell, W. (2009a). Lunar prospector measurements of secondary electron emission from lunar regolith. *Planetary and Space Science*, 57(1), 78–82. <https://doi.org/10.1016/j.pss.2008.11.009>

Halekas, J., Delory, G., Lin, R., Stubbs, T., & Farrell, W. (2009b). Lunar surface charging during solar energetic particle events: Measurement and prediction. *Journal of Geophysical Research*, 114, A05110. <https://doi.org/10.1029/2009ja014113>

Halekas, J., Poppe, A., Delory, G., Sarantos, M., Farrell, W., Angelopoulos, V., & McFadden, J. (2012). Lunar pickup ions observed by ARTEMIS: Spatial and temporal distribution and constraints on species and source locations. *Journal of Geophysical Research*, 117, E06006. <https://doi.org/10.1029/2012je004107>

- Halekas, J., Saito, Y., Delory, G., & Farrell, W. (2011). New views of the lunar plasma environment. *Planetary and Space Science*, 59(14), 1681–1694. <https://doi.org/10.1016/j.pss.2010.08.011>
- Harada, Y., Machida, S., Halekas, J., Poppe, A. R., & McFadden, J. P. (2013). ARTEMIS observations of lunar dayside plasma in the terrestrial magnetotail lobe. *Journal of Geophysical Research: Space Physics*, 118, 3042–3054. <https://doi.org/10.1002/jgra.50296>
- Harada, Y., Poppe, A. R., Halekas, J. S., Chamberlin, P. C., & McFadden, J. P. (2017). Photoemission and electrostatic potentials on the dayside lunar surface in the terrestrial magnetotail lobes. *Geophysical Research Letters*, 44, 5276–5282. <https://doi.org/10.1002/2017GL073419>
- Lin, R. P. (1968). Observations of lunar shadowing of energetic particles. *Journal of Geophysical Research*, 73(9), 3066–3071. <https://doi.org/10.1029/ja073i009p03066>
- Lin, R. P., & Gopalan, R. (1991). Mapping the composition of planetary surfaces by Auger electron spectroscopy. *Review of Scientific Instruments*, 62(3), 660–666. <https://doi.org/10.1063/1.1142064>
- Manka, R. H. (1973). Plasma and potential at the lunar surface. In *Photon and particle interactions with surfaces in space* (pp. 347–361). Springer. https://doi.org/10.1007/978-94-010-2647-5_22
- Manka, R. H., & Michel, F. (1973). *Lunar ion energy spectra and surface potential*. Pergamon Press.
- McCoy, J. E., Lin, R. P., McGuire, R. E., Chase, L. M., & Anderson, K. A. (1975). Magnetotail electric fields observed from lunar orbit. *Journal of Geophysical Research*, 80(22), 3217–3224. <https://doi.org/10.1029/ja080i022p03217>
- McFadden, J., Carlson, C., Larson, D., Ludlam, M., Abiad, R., Elliott, B., et al. (2008). The THEMIS ESA plasma instrument and in-flight calibration. *Space Science Reviews*, 141(1–4), 277–302. <https://doi.org/10.1007/s11214-008-9440-2>
- Mitchell, D., Lin, R., Rème, H., Crider, D., Cloutier, P., Connerney, J., et al. (2000). Oxygen auger electrons observed in Mars' ionosphere. *Geophysical Research Letters*, 27(13), 1871–1874. <https://doi.org/10.1029/1999gl010754>
- Pedersen, A. (1995). Solar wind and magnetosphere plasma diagnostics by spacecraft electrostatic potential measurements. *Annales geophysicae*, 13, 118–129. <https://doi.org/10.1007/s00585-995-0118-8>
- Poppe, A., Halekas, J. S., & Horányi, M. (2011). Negative potentials above the day-side lunar surface in the terrestrial plasma sheet: Evidence of non-monotonic potentials. *Geophysical Research Letters*, 38, L02103. <https://doi.org/10.1029/2010gl046119>
- Poppe, A., Halekas, J. S., Samad, R., Sarantos, M., & Delory, G. (2013). Model-based constraints on the lunar exosphere derived from artemis pickup ion observations in the terrestrial magnetotail. *Journal of Geophysical Research: Planets*, 118, 1135–1147. <https://doi.org/10.1002/jgre.20090>
- Poppe, A., & Horányi, M. (2010). Simulations of the photoelectron sheath and dust levitation on the lunar surface. *Journal of Geophysical Research*, 115, A08106. <https://doi.org/10.1029/2010ja015286>
- Poppe, A., Samad, R., Halekas, J., Sarantos, M., Delory, G., Farrell, W., et al. (2012). ARTEMIS observations of lunar pick-up ions in the terrestrial magnetotail lobes. *Geophysical Research Letters*, 39, L17104. <https://doi.org/10.1029/2012gl052909>
- Purucker, M. (2008). A global model of the internal magnetic field of the moon based on lunar prospector magnetometer observations. *Icarus*, 197(1), 19–23. <https://doi.org/10.1016/j.icarus.2008.03.016>
- Reasoner, D. L., & Burke, W. J. (1972). Characteristics of the lunar photoelectron layer in the geomagnetic tail. *Journal of Geophysical Research*, 77(34), 6671–6687. <https://doi.org/10.1029/ja077i034p06671>
- Richmond, N., & Hood, L. (2008). A preliminary global map of the vector lunar crustal magnetic field based on lunar prospector magnetometer data. *Journal of Geophysical Research*, 113, E02010. <https://doi.org/10.1029/2007je002933>
- Sternovsky, Z., Chamberlin, P., Horanyi, M., Robertson, S., & Wang, X. (2008). Variability of the lunar photoelectron sheath and dust mobility due to solar activity. *Journal of Geophysical Research*, 113, A10104. <https://doi.org/10.1029/2008ja013487>
- Stubbs, T. J., Vondrak, R. R., & Farrell, W. M. (2006). A dynamic fountain model for lunar dust. *Advances in Space Research*, 37(1), 59–66. <https://doi.org/10.1016/j.asr.2005.04.048>
- Tsunakawa, H., Takahashi, F., Shimizu, H., Shibuya, H., & Matsushima, M. (2015). Surface vector mapping of magnetic anomalies over the moon using kaguya and lunar prospector observations. *Journal of Geophysical Research: Planets*, 120, 1160–1185. <https://doi.org/10.1002/2014je004785>
- Walbridge, E. (1973). Lunar photoelectron layer. *Journal of Geophysical Research*, 78(19), 3668–3687. <https://doi.org/10.1029/ja078i019p03668>
- Willis, R. F., Anderegg, M., Feuerbacher, B., & Fitton, B. (1973). Photoemission and secondary electron emission from lunar surface material. In R. J. L. Gard (Ed.), *Photon and particle interactions with surfaces in space* (pp. 389–401). Dordrecht, Springer Netherlands. https://doi.org/10.1007/978-94-010-2647-5_25
- Xu, S., Thiemann, E., Mitchell, D., Eparvier, F., Pawlowski, D., Benna, M., et al. (2018). Observations and modeling of the mars low-altitude ionospheric response to the 10 september 2017 X-class solar flare. *Geophysical Research Letters*, 45, 7382–7390. <https://doi.org/10.1029/2018GL078524>
- Xu, S., Weber, T., Mitchell, D. L., Brain, D. A., Mazelle, C., DiBraccio, G. A., & Espley, J. (2019). A technique to infer magnetic topology at Mars and its application to the terminator region. *Journal of Geophysical Research: Space Physics*, 124, 1823–1842. <https://doi.org/10.1029/2018ja026366>
- Yokota, S., Saito, Y., Asamura, K., Tanaka, T., Nishino, M. N., Tsunakawa, H., et al. (2009). First direct detection of ions originating from the moon by map-pace ima onboard selene (kaguya). *Geophysical Research Letters*, 36, L11201. <https://doi.org/10.1029/2009gl038185>